Planform Geometric Variation, and its Effect on the Autorotation Efficiency of a Mechanical Samara

Evan R. Ulrich[ε], Darryll J. Pines[π]
Alfred Gessow Rotorcraft Center
Department of Aerospace Engineering
University of Maryland
College Park, MD 20742
evanu@umd.edu[ε], pines@umd.edu[π]

[ε] Graduate Research Assistant

[π] Professor

Presented at the American Helicopter Society 64th Annual Forum, Montréal, Canada, April 29 - May 1, 2008.

Abstract

An experimental methodology intended to characterize the autorotation efficiency and vehicle dynamics of Samara-like MAVs is presented. The scale inherent in these vehicles precludes the use of most conventional in situ sensors, and so data collection is limited to external observation. The studies presented herein demonstrate a new technique for collecting flight data from a vision based motion capture system. A test apparatus has been constructed to yield repeatable initial conditions, minimizing uncertainty of the Samaras dynamic state prior to data collection. The test specimen are constructed of an ultra-violet cured liquid polymer, which is dispensed and cured via the use of rapid prototyping machine. The use of this machine allows damaged subjects to be discarded and replaced with one of identical characteristics, ensuring the similarity of the models tested. This work is of interest as it relates to theoretical predictions of descent velocity, and its dependence on wing loading. The mechanical Samaras in this study are compared on the basis of equal wing loading. The results of these experiments identify an optimal geometry for minimal descent rate, as well as producing a quantitative Fourier series representation of the roll and pitch. Additionally, a new relationship has been established which allows for the prediction of descent velocity, as well as radius of precession. This information will aid in the development and validation of an inflow model for the mechanical Samara.

Introduction

Samaras, or winged seeds, are the sole method by which several species of plants propagate their seed. Geometric configurations for maximal seed dispersal has evolved into two main classes of seeds. Both of which execute autorotational flight as they fall from the tree, and one of which additionally rotates about its longitudinal axis. This discussion is limited to Samaras which execute only autorotational flight.

Advancements in technologies associated with the sensing and control aspect of unmanned vehicles has allowed conventional micro-scaled vehicles to be equipped with real-time systems. The vast capabilities provided to these small systems is limited by the battery life and power consumption of all on-board electronics and actuators. The majority of the power consumed in an aerial system is sustaining a desired flight mode. The primary focus of this flight mode is to negate the effects of gravity. Perhaps a new paradigm is needed, whose focus is the design of a vehicle with a passively stable primary mode of operation, one which requires little or no additional power to attain/maintain this mode of transit. The natural flight of a Samara is one of elegance and balance; trading gravitational potential energy for rotational kinetic energy which perpetuates an aerodynamically stable helical descent.

In nature the phenomenon of autorotation is utilized by various species of trees. The optimality of the autorotation heavily influences the population dynamics. The evolution of the Samara provides a near infinite set of feasible autorotation configurations, each with distinct dynamics. The goal of this work is to characterize the impact of span-wise chord variation on the descent velocity, and attitude dynamics. This will provide a baseline for mechanical Samara planform design. Additionally insight into the locations of lift production will be obtained. This information will aid the development and verification of a dynamic/aerodynamic six degree of freedom mechanical Samara model.

Previous work in this field has characterized surface roughness, center of gravity placement, leading edge thickness, and planform design[1,2,3]. These studies are however limited in scale (< 1 gram) and accuracy. The majority of the work to date describes the mechanisms of flight for natural Samaras, which presently are incapable of supporting any useful payload. The simulated mass considered here corresponds to that of an embedded electronics package ~ 5 grams.

Experimental Setup:

To capture the flight path of the mechanical Samara the VICON vision system is used[4]. The system collects data by capturing 2D images of the subject which is fitted with retro-reflective markers. The VICON system strobes light at the frame rate of the camera. The light incident on the surface of the marker returns to its source, reducing errors commonly caused by interference. The light returned to the lens allows for a quick computation of the centroid of the marker. Three-dimensional position is obtained from triangulation of camera observations. The setup of the workspace is tracked real time by the VICON system, the simulated workspace can be seen in Figure 2,3. The cameras are labeled one through seven, and are placed around the test area, Figure 1.

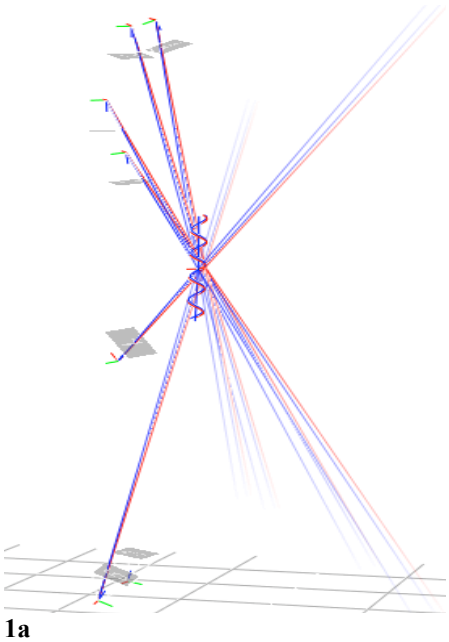

1a

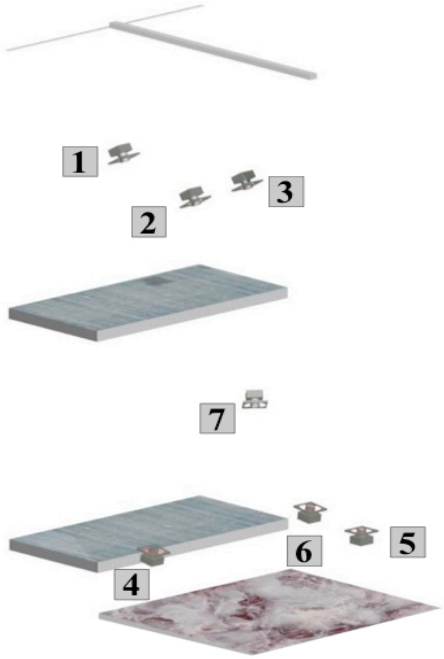

1b

Figure 1a:Vicon Ray traces a Samara in flight; 1b: 3-View of test area with cameras labeled 1-7.

A simple mechanical release mechanism is used to hold the mechanical Samara at a predetermined angle. The grip is grooved to ensure exact placement of the Samara for each drop test. This release mechanism is mounted ~12m above the ground, and is released after transient motion has been eliminated with the physical contact the mechanism makes with the platform mounted to the ceiling. The Samara is placed into the gripper, and hoisted to the ceiling by an attached thread of monofilament, which drapes over a pulley and back down to the ground, where it is attached to a fishing rod.

Pulley & Abutted Claw **Claw grasping a Samara**

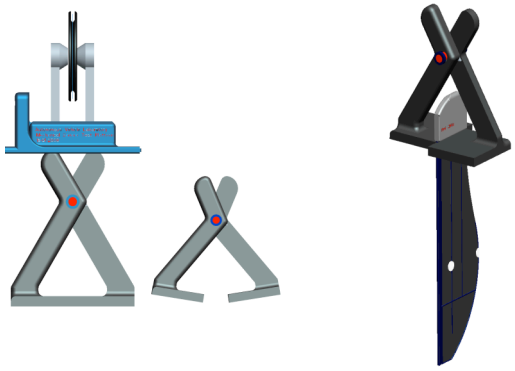

2a **2b** **2c**

Figure 2a: Release mechanism 'closed' and in contact with platform; 2b: claw in 'open' position; 2c: Claw 'closed' grasping NAVE A41.

In order to minimize wind disturbances which may effect the flight dynamics, these experiments were conducted in a room which had no ventilation. The test facility encompassed two platforms which provided the area for camera placement. The viewing angle of the cameras is critical in capture as well as calibration of the system. A minimum of three cameras are needed to calibrate the ground floor plane. This step in the calibration dictates the skew, if any, of the vertical axis. To avoid potential pitfalls from a poorly calibrated ground-floor-plane, markers are distributed in the area of interest, and the VICON system takes an average of the location of the markers which enhances the previously calibrated floor-plane. This calibration gives the user a least squares estimate of the error associated with the tracking of each marker. Tracking errors for the trials included here are less than 1mm of position uncertainty.

Each subject is calibrated for exact marker placement, including its possible range of motion. This accounts for dissimilar marker placement between trials and subjects. The algorithm used to correlate marker position uses this information in the event a marker is temporarily out of the field of view of at least two cameras. In some instances, manual marker labeling is required.

The marker placement is done in such a fashion as to interfere minimally with the aerodynamics of the subject. The subjects are designed with grooves which trace the outline of intended marker location, ensuring similar marker placement between subjects and trials. Typical marker geometry is spherical, and at the very least highly three-dimensional. The use of non-standard markers for these experiments is chosen with the intention of interfering minimally with the aerodynamics. The markers are made of retro-reflective tape provided by VICON, and manufactured by 3M. A hole-punch is used to ensure similarity of marker dimension, and the markers are made approximately three-dimensional by placing markers symmetrically on both sides of the Samara. Three markers are placed on the Samara permitting attitude determination. Marker placement for the rigid body model is shown in figure 3 in VICON inertial coordinates, note the three markers are coplanar.

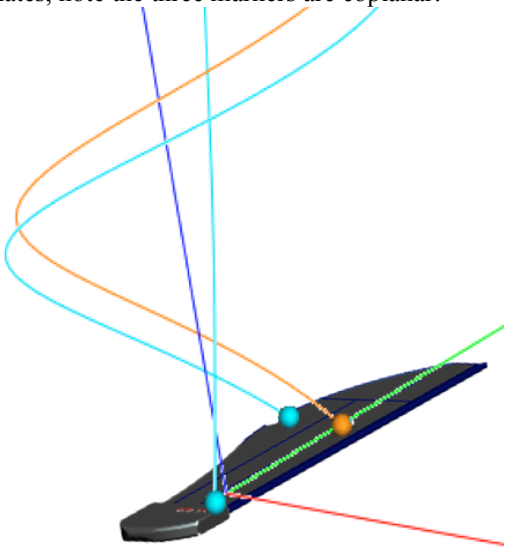

3a

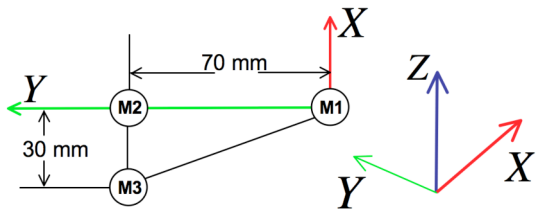

3b

Figure 3a: Mechanical Samara displaying labeled markers and trajectories. b: Marker placement and definition with VICON Inertial axes coordinate system

When working with the VICON software it is necessary to define a rigid body model which defines the degrees of freedom of each of the segments of the subject. This helps to ensure only physically possible solutions are converged upon in the post processing of a trial. The definition of a rigid body is done so with a fixed body coordinate system, hence the Euler angles reported for a clockwise descent are different then those of a counterclockwise descent. It is thus necessary to do an additional rotation of π about the fixed body X-axis to avoid the singularity this introduces in the calculation of the orientation.

Physical Model: The models are designated by the planform geometry A41, B41, C41 and D41. The geometry of the models tested are not simple scaled-up versions of natural Samaras. The design involved a trial and error method, aimed at producing a mechanical Samara capable of being tested in the limited space of the laboratory; the main constraint being the height of the ceiling.

Each subject is designed with identical cross-sectional properties which include: thick leading edge, 1.54 mm, followed by .1 mm region that extends to the trailing edge, Figure 3. Each cross section contains longitudinal stiffeners which appear as .55mm, .6 mm, and .85 mm circles, from left to right, on the airfoil cross section.

Figure 6: Mechanical Samara airfoil cross-section

The models were designed using CAD software capable of calculating precisely the model surface area and the location of the center of mass as well as overall model mass. These parameters are held constant over the four different subjects, Figure 5.

The CAD model can then be exported as a stereo-lithography file (STL), which is a representation of the Samaras geometry as approximated by triangles of varying dimension. This file is then used by the Eden350 to create the physical prototype. The tolerances of the machine are 42 micro-meters in the X-Y plane, and 16 micro-meters in the Z-plane[5]. Subjects are built in the same orientation on the machine to ensure similarity between models.

Design of the mechanical Samara involves precise placement of the center of mass, as a poor choice results in a less stable and efficient autorotation. It has been found to be advantageous to include a thick leading edge. In previous experiments, this has resulted in a 33% decrease in decent velocity[1]. In the same study increased surface roughness decreased the descent velocity. The mechanical Samara designed for these experiments exhibit a smooth surface finish.

The mechanical Samara tested have the physical properties listed in Table 1. It should be noted that all mechanical Samara are planar symmetric, hence zero twist. The inertias reported here lack the final addition of the marker mass, however the final mass does include this addition.

Table 1: Physical Properties of the mechanical Samara

NAVE		A41	B41	C441	D41
1st Principal Inertia	I_{11} Kg•m^2	8.99e^{-6}	6.92e^{-6}	9.32e^{-6}	6.93e^{-6}
2nd Principal Inertia	I_{22} Kg•m^2	4.39e^{-7}	5.05e^{-7}	4.5e^{-7}	5.99e^{-7}
3rd Principal Inertia	I_{33} Kg•m^2	9.42e^{-6}	7.41e^{-6}	9.76e^{-6}	7.52e^{-6}
Radius	m	.1686	.15	.1683.	.1359
Mass	Kg	.0526	.0526	.0526	.0526
Surface Area	m^2	1.24e^{-2}	1.24e^{-2}	1.24e^{-2}	1.24e^{-2}

The geometry of the planform area can be represented through Fourier series approximation of the chord as it varies with the radius, as seen in Figure 4. Each of the approximated geometries are reported with the mean square fit error.

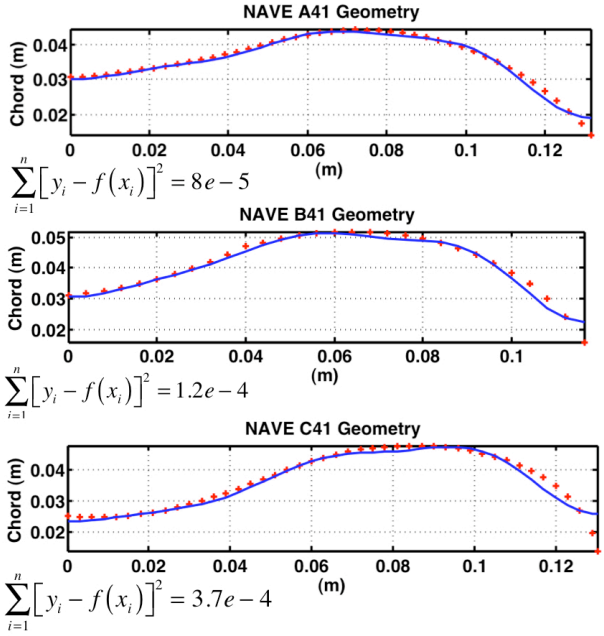

Figure 4: Samara geometry approximated by a Fourier cosine series.

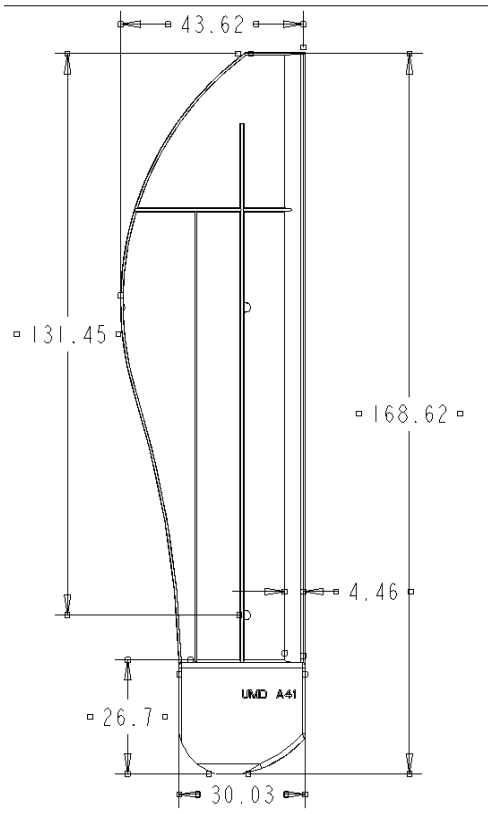

NAVE A41

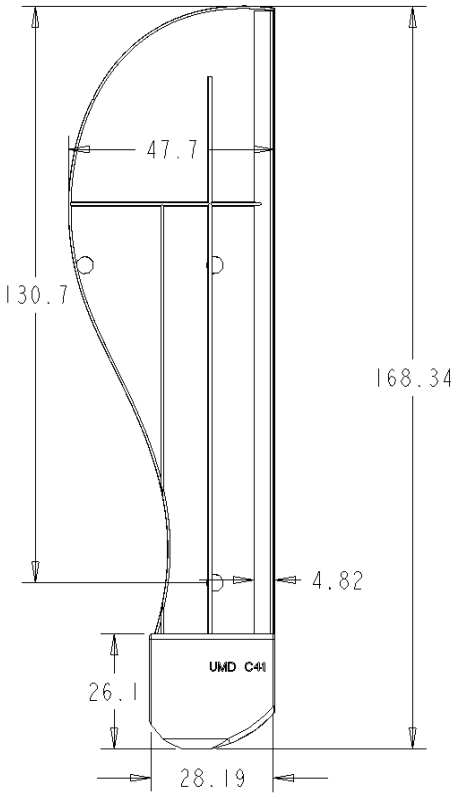

NAVE C41

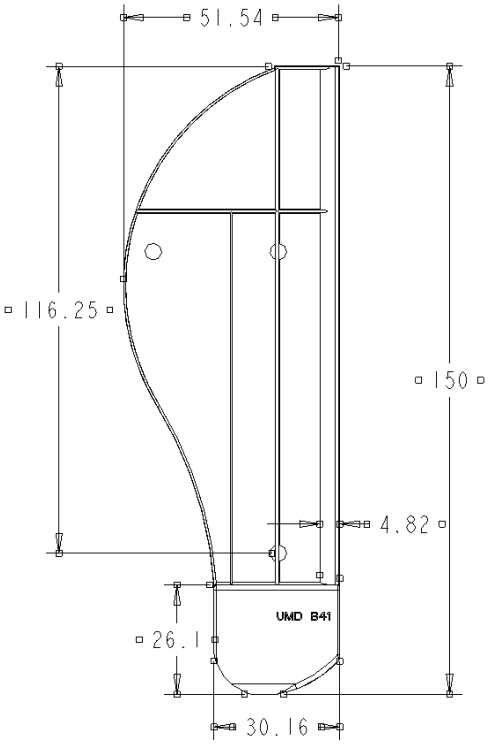

NAVE B41

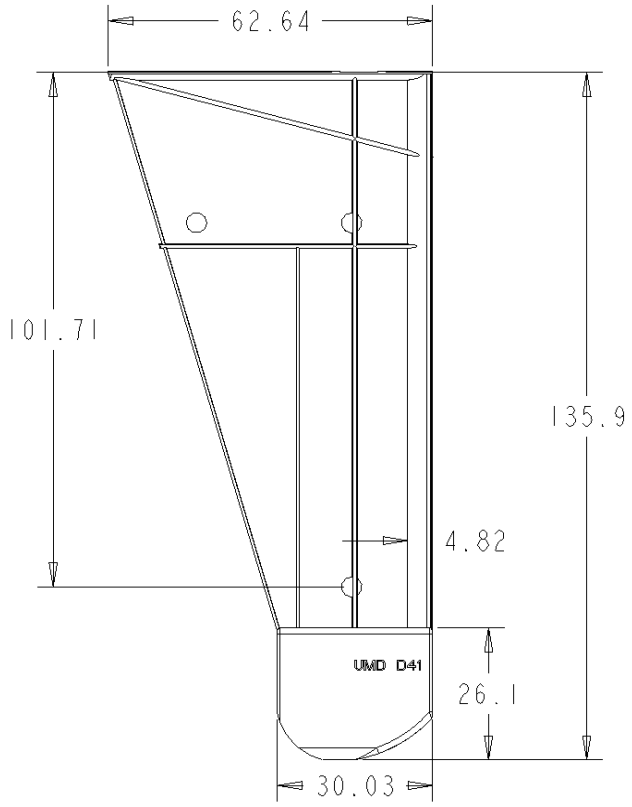

NAVE D41

Figure 5: Schematic of test subject geometry, all dimensions in mm.

The coefficients of the Fourier series corresponding to the above geometries is detailed in Table 2, for the series:

$$\Phi(t) = a_o + \sum_{n=1}^{6} a_n \cos n\omega_o t \qquad (1)$$

Table 2: Fourier series coefficient for Samara geometry.

Samara Model			
Fourier Coefficients	A41	B41	C411
a_o	.0358	.0414	.0362
a_1	.001	-.0006	-.0071
a_2	-.0084	-.0113	-.0085
a_3	.0032	.0029	.004
a_4	-.0017	-.0024	-.0017
a_5	.0012	.0019	.0019
a_6	-.0011	-.0012	-.0013

The Geometry of the NAVE D41 model is simple and can calculated from the schematic provided in Figure 5.

Data Reduction and Analysis

Attitude Representation: Subsequent testing of the various Samara provided an insight into the governing dynamics as they varied with the geometry.

Attitude representation requires separate basis for the fixed inertial axes (F) and the body axes which is fixed to the Samara (B).

$$F = \left\{\hat{f}_x, \hat{f}_y, \hat{f}_z\right\} \qquad (2)$$

$$B = \left\{\tilde{e}_i, \tilde{e}_j, \tilde{e}_k\right\} \qquad (3)$$

$$\left[\vec{r}\right]_B = R_1(\phi) \bullet R_2(\theta) \bullet R_3(\psi) \bullet \left[\vec{r}\right]_F \qquad (4)$$

The transformation from the inertial frame to that of the body frame is described by three Euler angles. The order of rotation is as follows: a 'yaw' rotation ψ about the $\hat{f}_z$ axis, followed by a 'pitch' rotation θ, about the new $\hat{f}_y$ axis, and lastly a 'conning' rotation ϕ, about the new $\hat{f}_x$ axis. The transformation matrix can then be written as:

$$R_{BF} = \begin{bmatrix} c\psi c\theta & s\psi c\theta & -s\theta \\ c\psi s\theta s\phi - s\psi c\phi & c\psi c\phi + s\psi s\theta s\phi & c\theta s\phi \\ s\psi s\phi + c\psi s\theta c\phi & s\psi s\theta c\phi - c\psi s\phi & c\theta c\phi \end{bmatrix} \qquad (5)$$

The notation is such that $s\theta = \sin\theta$, and $c\theta = \cos\theta$.
This rotation sequence is standard for aircraft[6]; the diagram for which is shown in Figure 7.

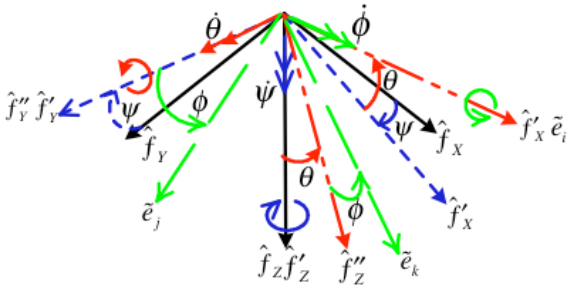

Figure 7: Rotation sequence, Inertial coordinates to body fixed coordinates.

The Euler angular rates are defined in the inertial coordinate system, Figure 7. The angular rates in the inertial frame are finite rotations, which do not commute, it is thus necessary to define the body angular rates separately. The sum of the inner products of each of the inertial angular rates with the body axis of interest yields the body angular rates Eq[6-9].

$$p = -\dot{\psi}\sin\theta + \dot{\phi} \qquad (6)$$

$$q = \dot{\psi}\cos\theta\sin\phi + \dot{\theta}\cos\phi \qquad (7)$$

$$r = \dot{\psi}\cos\theta\cos\phi - \dot{\theta}\sin\phi \qquad (8)$$

A schematic detailing the axis of these rotations is shown in Figure 8.

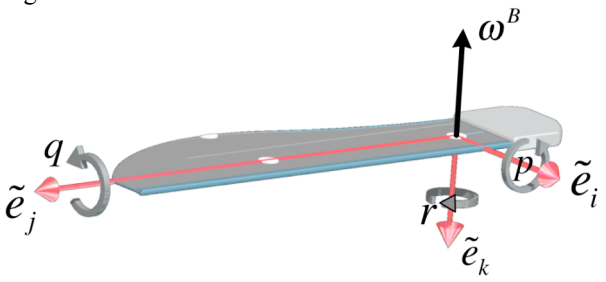

Figure 8: Roll, Pitch and Yaw definitions for body fixed coordinate system.

The 3D marker position data provides a means of resolving the orientation of the mechanical Samara in space. The three markers are sufficient to describe an orthonormal basis from which the rotation matrix representing the Samaras orientation can be formed.

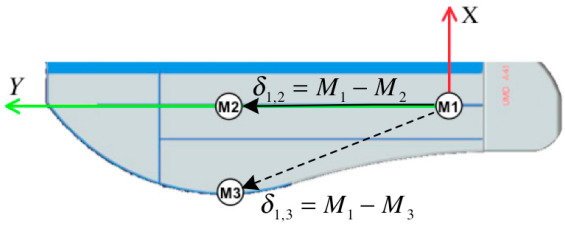

Figure 9: Samara marker placement and definition (VICON body fixed coordinate frame)

The first vector forms the $\tilde{e}_j$-axis in body frame coordinate and is the line from the Samara center of mass to the marker located ~70mm in the positive VICON Y-direction. The remaining basis require an intermediate vector

from which to compute a cross product defining the $\tilde{e}_k$-axis as follows:

$$\delta_{1,2} = M_1 - M_2 \tag{9}$$

$$\delta_{1,3} = M_1 - M_3 \tag{10}$$

$$\nu = \frac{\delta_{1,3}}{\|\delta_{1,3}\|} \tag{11}$$

The intermediate vector $\delta_{1,2}$ can be normalized forming the $\tilde{e}_i$ body frame axis. The vector ν is formed by normalizing $\delta_{1,3}$, this vector is the used to compute the body frame $\tilde{e}_k$ axis. The final body axis is formed in the cross product of $\tilde{e}_k$ and $\tilde{e}_i$. This set form the orthonormal basis which defines the orientation of the body with respect to the inertial frame. The rotation matrix A is formed with each column defined by one of the basis vectors. The entries of the A matrix are:

$$A = \begin{bmatrix} \alpha_{11} & \alpha_{12} & \alpha_{13} \\ \alpha_{21} & \alpha_{22} & \alpha_{23} \\ \alpha_{31} & \alpha_{32} & \alpha_{33} \end{bmatrix} \tag{12}$$

The elements of the matrix are found in the computation of the basis,

$$\tilde{e}_i = \frac{\delta_{1,2}}{\|\delta_{1,2}\|} = \alpha_{11} + \alpha_{21} + \alpha_{31} \tag{13}$$

$$\tilde{e}_j = \tilde{e}_k \times \tilde{e}_i = \alpha_{12} + \alpha_{22} + \alpha_{32} \tag{14}$$

$$\tilde{e}_k = \nu \times \tilde{e}_i = \alpha_{13} + \alpha_{23} + \alpha_{33} \tag{15}$$

This matrix exhibits the normal properties of a rotation matrix; the determinant is unity, and so the transpose is equal to the inverse:

$$\det(A) = \pm 1 \tag{16}$$

$$AA^T = \mathrm{I} \tag{17}$$

Once three-dimension marker position is obtained and the basis set of the Samara body axes are computed, the Euler angles can be deduced from the newly formed rotation matrix [A]. The Euler angles provide a non-unique set of rotations which can describe the Samaras orientation, however a singularity arises near $\theta = \pm\pi/2$. Away from the singularity the angles are as follows:

$$\theta = \arcsin(-\alpha_{13}) \tag{18}$$

$$\psi = \arctan(\alpha_{11} / \alpha_{12}) \tag{19}$$

$$\phi = \arctan(\alpha_{23} / \alpha_{33}) \tag{20}$$

The use of the MATLAB function atan2, the four quadrant arctangent of the real component of the arguments in the range of $-\pi \le \arctan 2(\alpha_1, \alpha_2) \le \pi$, is needed to retain continuity of signs between successive time steps. The limited range of the arctan2 calculation is a short-coming of the Euler angle attitude representation which requires special treatment of the remaining rotations near the singularity. A simple and effective solution is to set the angle $\psi = 0$, leaving the final angle ϕ as:

$$\phi = \arctan(\alpha_{21} / \alpha_{31}) \tag{21}$$

The Euler angles ϕ and θ display periodic behavior and are roughly 90° out of phase with one another. This is to be expected as 'pitching' leads 'conning' by 90° in full scale helicopters. This implies the maximum force on the Samara θ_{max}, displaces the Samara maximally $\phi_{\max}$, one quarter revolution later. This cyclic behavior can be seen in Figure 10.

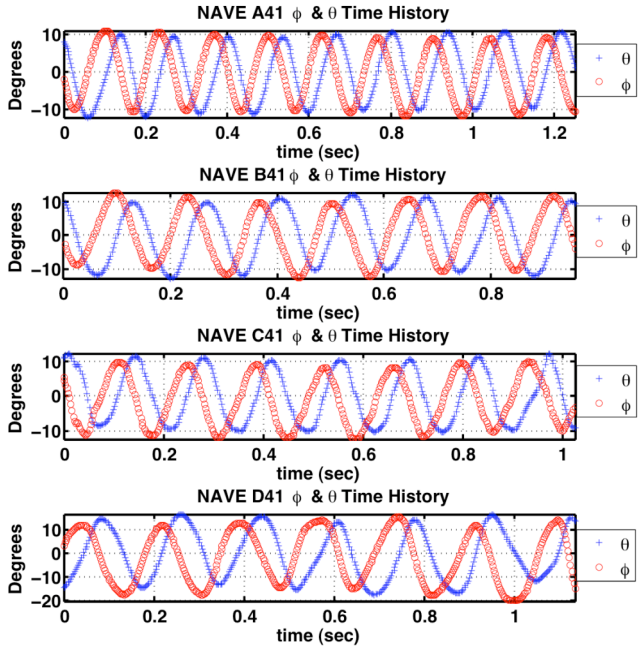

Figure 10: Euler angle time history for NAVE A-D41

The scope of flight in this study is characterized by a nearly constant radius of precession, or more precisely a standard deviation, σ_r, of no more than 6.25% of the mean. The radius of precession is computed in cylindrical coordinates where $r_i = \sqrt{x_i^2 + y_i^2}$, where (x_i, y_i) denote the location of the center of mass of the Samara, or M1 from Figure 9. This parameter is the conciseness of the helical descent trajectory, such that a larger r_i implies a larger amount of transverse motion. The tabulated data shown in table 3, identify some key performance parameters, namely optimal geometry for minimal descent. The Samara rotate about the center of mass or CG, resulting in the majority of the wing area being located on one side oft the CG. The distance of the area centroid of this portion of the Samaras are calculated with respect to the CG and shown in table 4.

$$dz(y) = \lambda_1 y - \lambda_2 \tag{22}$$

$$r_{CG}(x) = \lambda_1 x^2 + \lambda_2 x + \lambda_3 \tag{23}$$

Table 3: Curve Fit parameters for dz(y) and $r_{CG}(x)$

	λ_1 (mm)	λ_2 (mm)	λ_3 (mm)
$dz(y)$ (m/s)	-.0211	.3324	n/a
95% Confidence	-.0298	-0.876	n/a
Bounds	-.0124	0.212	n/a
$r_{CG}(x)$ (mm)	-5.415	150.9	-509.5
95% Confidence	-7.325	125	-593
Bounds	3.505	176.8	-426

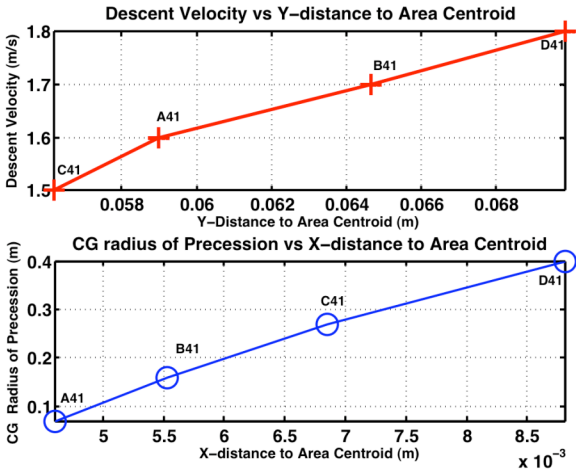

Figure 11: Influence of Area Centroid on descent velocity and radius of precession

Note the centroid location farthest fro the CG corresponds to the Samara which as well has the lowest descent velocity. Another characteristic elucidated by the area centroid location is the radius of precession of the CG. There is a quadratic relationship between the X-distance of the area centroid from the CG, and the radius of precession of the CG. These relationships are shown in Figure 11, and the curve fitting parameters are listed in Table 3. This relationship suggests the wing area centroid is a first cut estimate of the center of lift.

Table 4: Flight performance metrics

	r	σ_r	dr	σ_{dr}	dz	σ_{dz}	X	Y
NAVE	**m**	**m**	**m/s**	**m/s**	**m/s**	**m/s**	**mm**	**mm**
A41	.07	0	.31	.03	*-1.6*	.01	4.6	*64.6*
B41	.16	.01	.06	.02	*-1.7*	.02	6.9	*59.0*
C41	.27	.01	.09	.04	*-1.5*	.06	5.5	*69.8*
D41	.40	.02	.10	.05	*-1.8*	.05	8.8	*56.2*

The standard deviation which is a function of the sample variance is computed as:

$$\sigma = \sqrt{\frac{1}{N}\sum_{i=1}^{N}(x_i - \bar{x})^2} \qquad (24)$$

Where $\bar{x}$ is the sample mean;

$$\bar{x} = \frac{1}{N}\sum_{i=1}^{N} x_i \qquad (25)$$

x_i is the local value of the parameter, thus the units of σ are the same as those of x_i.

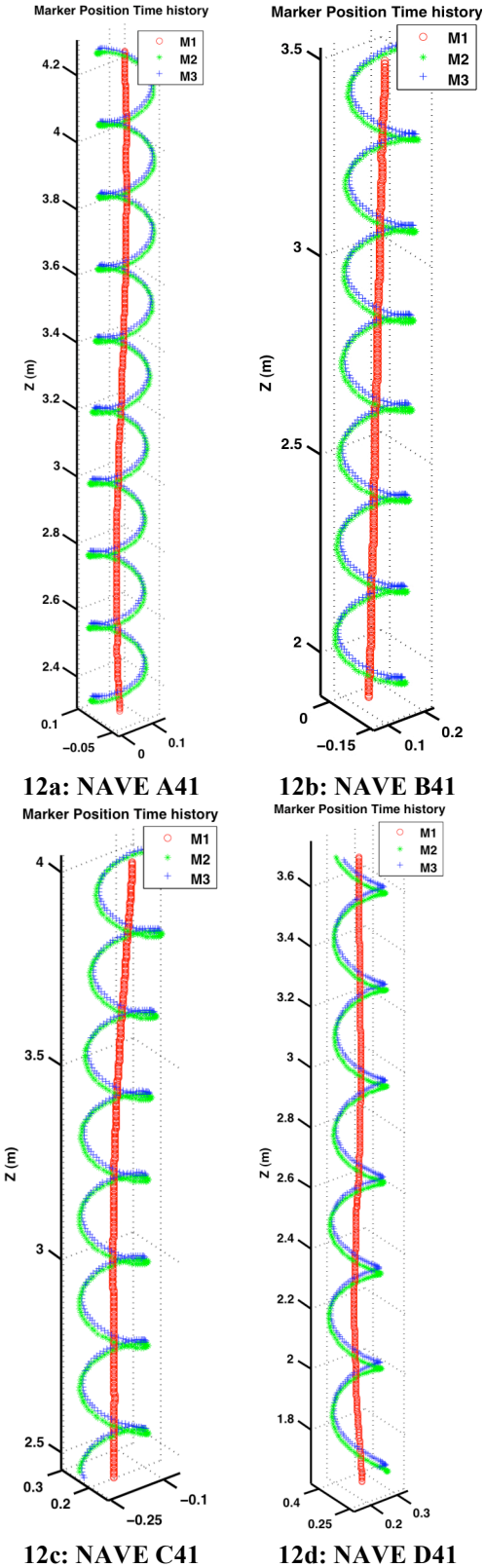

12a: NAVE A41 **12b: NAVE B41**

12c: NAVE C41 **12d: NAVE D41**

Figure 12a-d: Flight path of the various geometries. The marker definitions, M1-3 correspond to those defined previously in Figure 9. Note all dimensions are in meters.

The flight path and the Samara, as recorded by VICON is shown in Figure 12a-d. The center of mass is shown in red.

In applications involving periodic signals it is desirable to enhance signal to noise ratios in order to extract representative waveforms. Signal averaging techniques[7,8] previously implemented in applications such as structural health monitoring[9] and optical filter design[10], are employed here as a means of reducing a periodic signal into one discernable waveform. For a deterministic signal x(t) of period T, a measurement model can written as:

$$z(t)=x(t)+\nu(t) \tag{25}$$

Where $\nu(t)$ is additive sensor noise. For x(t) measured over N periods, the ensemble average and ensemble variance can be approximated as:

$$\eta_z(t)=\frac{1}{N}\sum_{n=0}^{N-1} z(t+nT) \tag{26}$$

$$\sigma_z^2(t)=\frac{1}{N}\sum_{n=0}^{N-1}\left[z(t+nT)-\eta_z(t)\right]^2 \tag{27}$$

Confidence intervals for estimated parameters can be formulated from estimation theory[11]. The 95% confidence interval of these measurements with regard to the signal averages is approximated as:

$$Z_{0.95}(t)=\eta_z(t)\pm 1.96\sigma_z(t) \tag{28}$$

This average is then described for each Samara by Fourier Sine or Cosine series of varying order. The specific parameters used for the ensemble averaging are listed in table 5.

Table 5: Time synchronous average parameters for each of the subjects tested.

NAVE		*f* Hz	T sec	points	N
A41	**p**	7.25	.137	500	8
	q	7.25	.138	500	8
B41	**p**	7.27	.138	384	6
	q	7.41	.135	384	6
C41	**p**	7.32	.137	411	7
	q	7.32	.137	411	7
D41	**p**	5.71	.175	455	6
	q	5.71	.175	455	6

The roll, pitch and yaw time history for each of the subjects is displayed in Figure 13a-16a. Following the time histories is the ensembles overlaid in blue, with signal average in black. The 95 % confidence interval is the dashed red line. The confidence interval bounds tends to increase from Samara A-D. Possible causes for this include but are not limited to; structural vibrations; susceptibility to small wind disturbance; and decreased aerodynamic damping resulting from a change in the center of pressure.

The number of ensembles averaged is highly dependent on the settling time of the individual Samara, and the limited drop height. This number could be increased at the cost of uncertain initial conditions by giving the Samara a pre-spin upon launch.

The bar graphs shown for each Samara indicate the presence and relative contribution of the individual modes to the roll and pitch rates. The yaw rate and curve fit are neglected here as the variation in amplitude is $\approx \pm 2$ rad/sec or 5% of the mean, and can be approximated with small error as a line.

$$p_A(t)=a_o+\sum_{n=1}^{8} a_n\cos n\omega_o t \tag{29}$$

$$q_A(t)=a_o+\sum_{n=1}^{5} b_n\sin n\omega_o t \tag{30}$$

$$p_B(t)=a_o+\sum_{n=1}^{8} a_n\cos n\omega_o t \tag{31}$$

$$q_B(t)=a_o+\sum_{n=1}^{5} b_n\sin n\omega_o t \tag{32}$$

$$p_C(t)=a_o+\sum_{n=1}^{8} a_n\cos n\omega_o t \tag{33}$$

$$q_C(t)=a_o+\sum_{n=1}^{5} b_n\sin n\omega_o t \tag{34}$$

$$p_D(t)=a_o+\sum_{n=1}^{8} a_n\cos n\omega_o t \tag{35}$$

$$q_D(t)=a_o+\sum_{n=1}^{5} b_n\sin n\omega_o t \tag{36}$$

The results of the Fourier analysis are tabulated and shown in Table 6. Note the significant presents higher order modes in the rotational dynamics.

Table 6: Fourier coefficients for roll and pitch

	ω_o	a_0/b_0	$a_1/b1$	$a_2/b2$	$a_3/b3$
Unit	Hz	rad	rad	rad	rad
$p_A(\omega_0 t)$	7.25	-.4885	-6.536	9.55	2.89
$q_A(\omega_0 t)$	7.25	0.1852	-.3729	-8.01	1.21
$p_B(\omega_0 t)$	7.27	-1.533	-7.74	8.05	3.9
$q_B(\omega_0 t)$	7.41	-.1067	-.065	-8.53	.006
$p_C(\omega_0 t)$	7.32	-.2538	-8.01	-6.053	3.797
$q_C(\omega_0 t)$	7.33	.9172	1.5976	7.892	-.1076
$p_D(\omega_0 t)$	5.71	-.257	7.0644	-7.64	-4.612
$q_D(\omega_0 t)$	5.71	1.99	4.22	10.1	-1.899

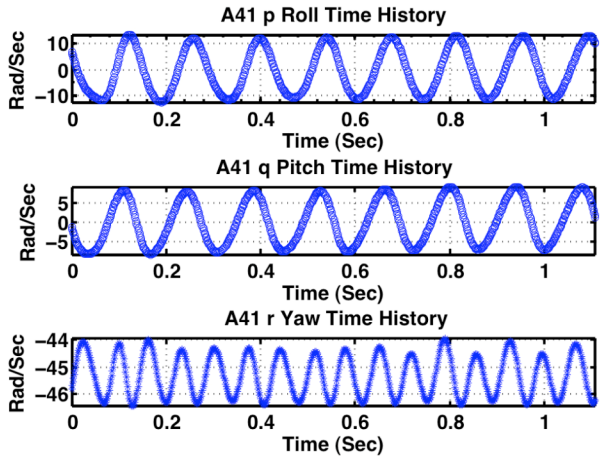

13a: NAVE A41 Time history of roll, pitch and yaw for steady descent;

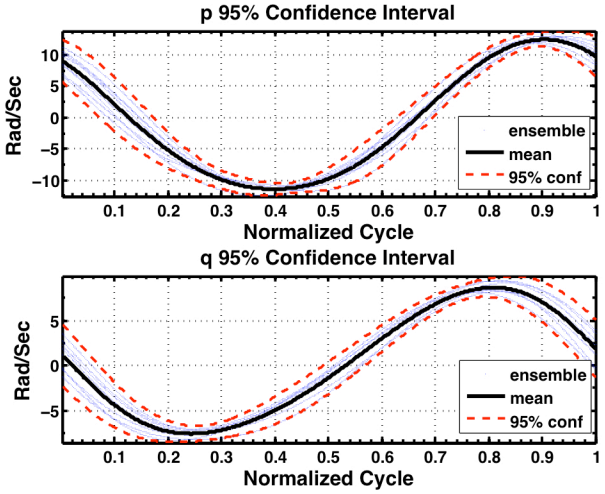

Figure 13b: NAVE A41 the time synchronous average roll and pitch;

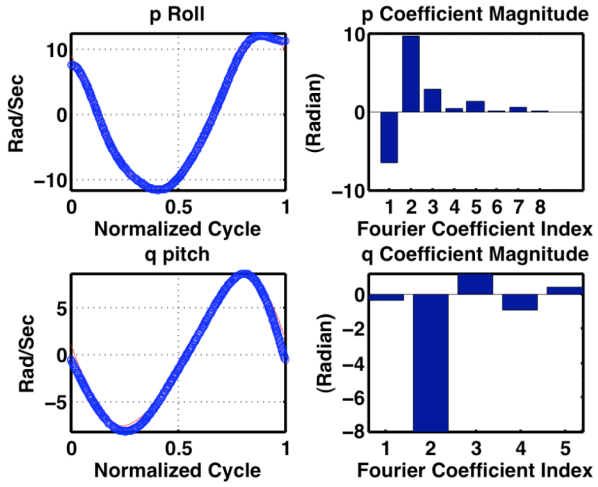

Figure 13c: Fourier decomposition of the roll and pitch time synchronous average.

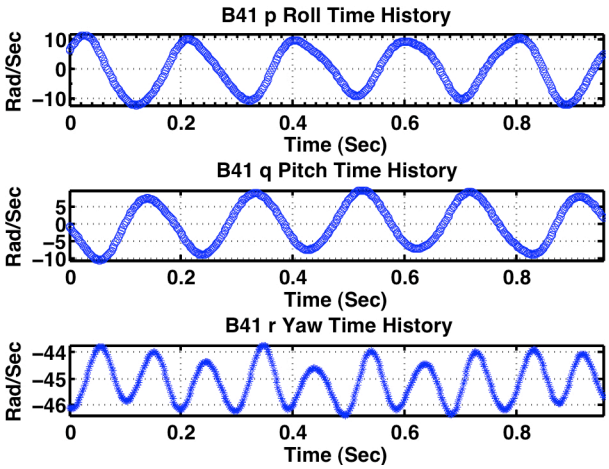

Figure 14a: NAVE B41 Time history of roll, pitch and yaw for steady descent;

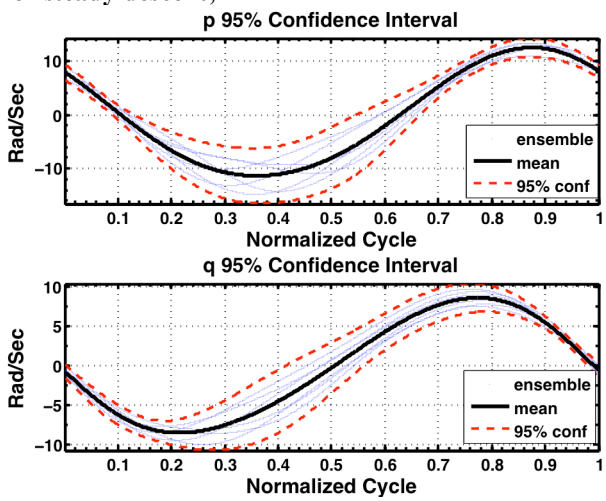

Figure 14b: NAVE B41 the time synchronous average roll and pitch;

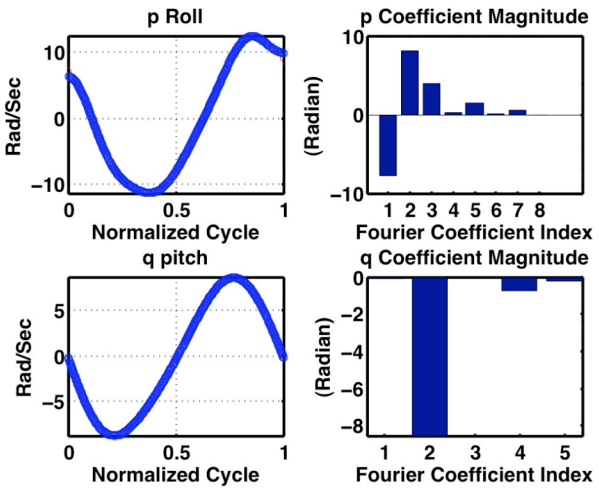

Figure 14c: NAVE B41 Fourier decomposition of the roll and pitch time synchronous average.

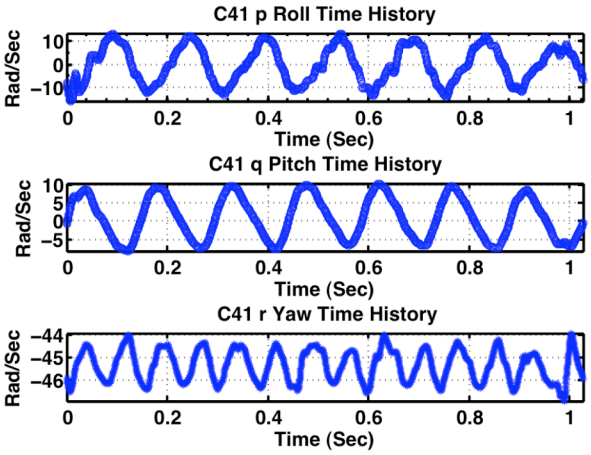

Figure 15a: NAVE C41 Time history of roll, pitch and yaw for steady descent;

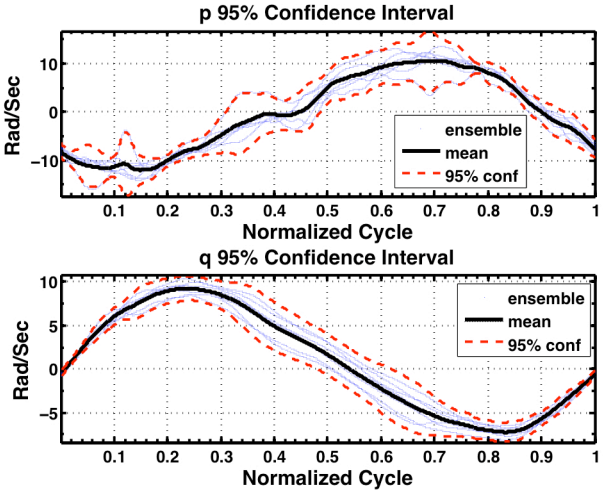

Figure 15b: NAVE C41 the time synchronous average roll and pitch;

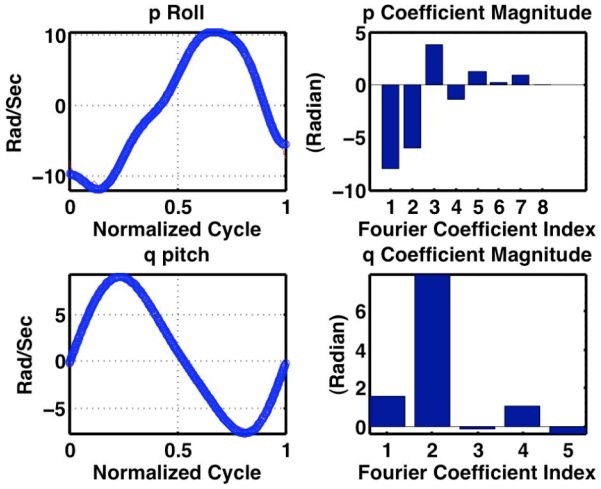

Figure 15c: NAVE C41 Fourier decomposition of the roll and pitch time synchronous average.

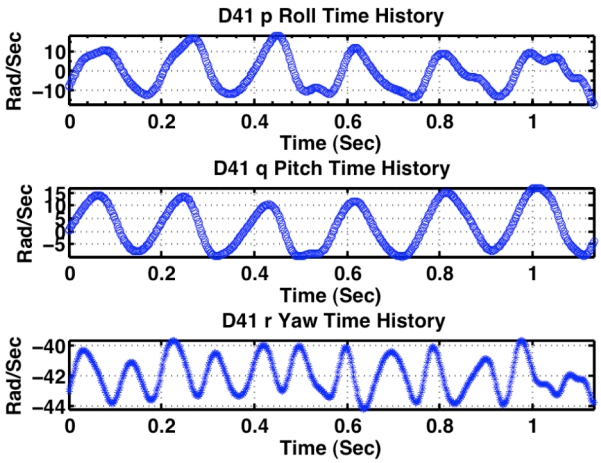

Figure 16a: NAVE D41 Time history of roll, pitch and yaw for steady descent;

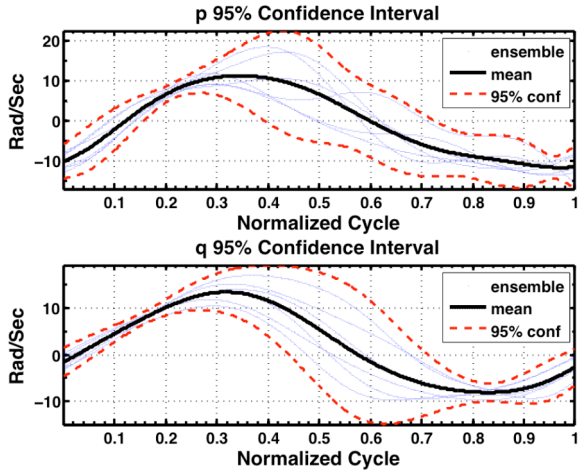

Figure 16b: NAVE D41 the time synchronous average roll and pitch;

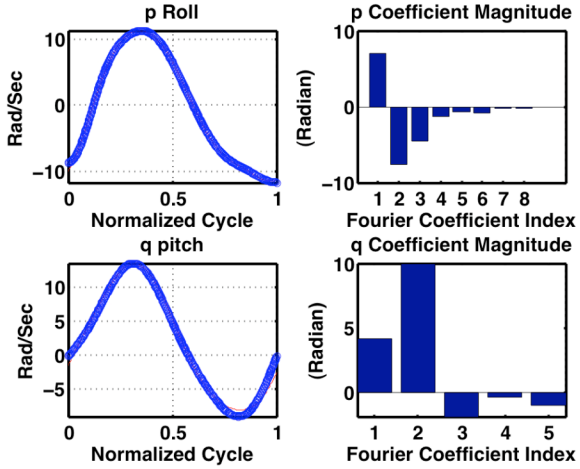

Figure 16c: NAVE D41 Fourier decomposition of the roll and pitch time synchronous average.

Conclusion:

The significant findings of this study are: 1.) Vision based motion capture is possible, and even preferred for the study of subjects at this scale, (4000<Re<9000); 2.) In steady vertical descent roll and pitch are neither constant nor

small as suggested in previous studies[2,3]. Those observation were most likely due to a lack of precision instrumentation, which has only recently become available. 3.) The planform geometry of the Samara tested resulted in a variation in descent velocity by as much as 16.7%, and clearly indicates a geometry for minimal descent velocity; NAVE C41 4.) Four new mechanical Samara designs have been presented, each capable of supporting a 5 gram electronics payload. 5.) A new Low Reynolds number airfoil has been presented and tested. This airfoil geometry has been proven to be effective over 4 variations in planform geometry. 6.) A new stability criterion for the flight of a mechanical Samara has been established, namely the standard deviation from the axis of precession of the center of mass. 7.) The radius of precession of the center of mass is highly variable, >500%, over the range of models tested. The Samara with the smallest radius of precession of the center of mass, as well displayed the smallest variation in roll, pitch, and yaw rates; 8.) A linear relationship has been established between the Y-distance of the area centroid and the descent velocity of the Samara. 9.) A quadratic relationship has been established between the X-distance of the area centroid and the radius of precession of the center of mass. These relationships parameterize the design space of the Samara planform, giving insight into the geometric nature of the underlying physics.

Acknowledgments

Thanks to the Faculty and staff of the University of Maryland for so graciously providing the facilities for these experiments. Thanks to Joseph Conroy and Jared Grauer for clarifying the intricacies of signal processing. Finally, thanks to Steve Gerardi and Joe Park for their tireless efforts in the design and testing phase of these experiments.

References

1.) A. Azuma, K. Yasuda. The Autorotation Boundary of the Flight of Samaras. Journal of Theoretical Biology, (1997) 185, 313-320.

2.) D. Seter, A. Rosen. Stability of the Vertical Autorotation of a Single-Winged Samara. Transactions of the ASME, Vol. 59, December 1992.

3.) D. Seter, A. Rosen. Vertical Autorotation of a Single-Winged Samara. Transactions of the ASME, Vol. 58, December 1991.

4.) Vicon Motion Systems Limited, www.vicon.com

5.) Objet Company, www.2objet.com : full cure materials data sheet; Vero Blue; Vero Black; FullCure 720.

6.) R. Stengel, Flight Dynamics; Princeton University Press, November 2004

7.) Orfanidis, S., Introduction to Signal Processing , Prentice Hall signal processing series, Prentice Hall, 2nd ed., August 1995.

8.) Hochmann, D. and Sadok, M., "Theory of Synchronous Averaging," IEEE Aerospace Conference Proceedings, Institute for Electrical and Electronics Engineers, 2004, pp. 3636–3653.

9.) Samuel, P. and Pines, D., "Helicopter Transmission Diagnostics using Constrained Adaptive Lifting," 59th Annual Forum, American Helicopter Society, Phoenix, AZ, 6-8 May 2003

10.) C. K. Madsen, J. H. Zhao, Optical Filter Design and Analysis ,Wiley Series in Microwave and Optical Engineering, 2001.

11.) Klein, V. and Morelli, E., Aircraft System Idenfication: Theory and Practice , AIAA Education Series, American Institute of Aeronautics and Astronautics,2006